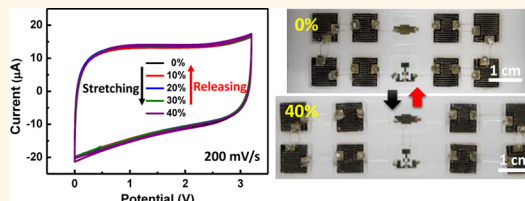# High-Density, Stretchable, All-Solid-State Microsupercapacitor Arrays

Soo Yeong Hong,[†] Jangyeol Yoon,[†] Sang Woo Jin,[‡] Yein Lim,[‡] Seung-Jung Lee,[§] Goangseup Zi,[§] and Jeong Sook Ha[*,†,‡]

[†]Department of Chemical and Biological Engineering, [‡]KU-KIST Graduate School of Converging Science and Technology, and [§]Department of Civil, Environmental and Architectural Engineering, Korea University, Seoul 136-701, Republic of Korea

ABSTRACT We report on the successful fabrication of stretchable microsupercapacitor (MSC) arrays on a deformable polymer substrate that exhibits high electrochemical performance even under mechanical deformation such as bending, twisting, and uniaxial strain of up to 40%. We designed the deformable substrate to minimize the strain on MSCs by adopting a heterogeneous structure consisting of stiff PDMS islands (on which MSCs are attached) and a soft thin film (mixture of Ecoflex and PDMS) between neighboring PDMS islands. Finite element method analysis of strain distribution showed that an almost negligible strain of 0.47% existed on the PDMS islands but a concentrated strain of 107% was present on the soft thin film area under a uniaxial strain of 40%. The use of an embedded interconnection of the liquid metal Galinstan helped simplify the fabrication and provided mechanical stability under deformation. Furthermore, double-sided integration of MSCs increased the capacitance to twice that of MSCs on a conventional planar deformable substrate. In this study, planar-type MSCs with layer-by-layer assembled hybrid thin film electrodes of MWNT/Mn_3O_4 and PVA-H_3PO_4 electrolyte were fabricated; when they are integrated into a circuit, these MSCs increase the output voltage beyond the potential of the electrolyte used. Therefore, various LEDs that require high voltages can be operated under a high uniaxial strain of 40% without any decrease in their brightness. The results obtained in this study demonstrate the high potential of our stretchable MSC arrays for their application as embedded stretchable energy storage devices in bioimplantable and future wearable nanoelectronics.

KEYWORDS: stretchable microsupercapacitor array · layer-by-layer assembly · high density · all-solid-state supercapacitor · embedded interconnection · liquid metal

R ecently, extensive research has been conducted on stretchable electronics that are applicable in various fields such as medical, environmental, and electronics industries.[1−3] In particular, the human body, including internal organs and skin, does not have flat surfaces; therefore, electronic devices should be deformable upon body movement. Thus, extensive efforts have been made to minimize the strain applied on active devices, process electronic devices on nonflat substrates, and maximize the fill factor of active devices.[4−11] As a result, it is expected that practical applications of stretchable electronics for the human body and wearable computers would be achieved in the near future.

With the increasing demand for personal and portable electronic devices, the need for embedded energy storage devices without any external wire connection to power sources has noticeably increased as well. Supercapacitors are considered as promising energy storage devices for digital communications and hybrid electronic vehicles because they have relatively simpler design and fabrication, deliver higher levels of electrical power, offer longer operating lifetimes, and are used more safely than batteries even though they still exhibit lower energy density.[12−19] In order to be used in stretchable electronics, supercapacitors should also be stretchable. However, until now, the stretchability of most supercapacitors depended on the elasticity of the constituent materials and the prestrain applied on the substrate, and this hindered the integration of supercapacitors into the circuits of stretchable electronics.[20−26] Designing planar-type supercapacitors made possible their integration into a circuit so that both the output operating voltage and total capacitance of the supercapacitor could be controlled *via* circuit design. In particular, patterning of the interspace between two planar electrodes in a supercapacitor on the micrometer scale can increase its capacitance by reducing the path length of ions in the

electrolyte; such a supercapacitor is called a micro-supercapacitor (MSC).[23−25] Furthermore, all-solid-state supercapacitors cannot use a liquid electrolyte and instead use a gel electrolyte.[27] As electrode materials with a large surface area and high electrical conductivity, carbon-based materials such as graphene and carbon nanotubes have been widely used.[28,29] In order to further increase the capacitance of supercapacitors via a redox reaction, combinations of metal oxide nanoparticles such as RuO_2,[30,31] NiO,[32,33] MnO_2,[34−36] and Mn_3O_4[37,38] have also been adopted. However, only a few reports have been published on stretchable MSCs. In our previous study,[39] we fabricated stretchable MSC arrays whose stretchability depended on curved suspended interconnections. However, the stretchability was limited by the ion-gel electrolyte covering the interconnections that could not stand repeated cycles of stretching and releasing.

In this study, we have successfully fabricated stretchable MSC arrays with stable electrochemical performance even upon repeated cycles of stretching and releasing. This stable performance can be attributed to our specially designed stretchable substrate. This substrate consists of relatively stiff island arrays (PDMS) for active devices on both sides of a soft thin film (mixture of Ecoflex and PDMS), and the active devices are electrically connected by embedded liquid metal interconnections of Galinstan. With this arrangement, the strain on the active devices was minimized and all of the strain was accommodated by the soft thin film. Owing to the presence of embedded interconnections, the electrochemical performance of the MSCs did not deteriorate even upon repeated deformation such as stretching, bending, and twisting. In addition, the areal density of the MSCs was twice that of MSCs on a planar substrate, since the MSCs could be integrated on islands on both sides of the substrate. Further, we used hybrid MWNT/Mn_3O_4 film electrodes in the MSCs and employed the layer-by-layer (LbL) method, which is a simple and extensively applied method for achieving large-area growth of various materials with a thickness controllable on the nanometer scale, for fabricating the electrodes. Subsequently, we integrated the fabricated all-solid-state planar-type MSCs with a PVA-H_3PO_4 electrolyte into a circuit with a serial connection and obtained a higher output voltage than the potential of the electrolyte. This enabled us to operate LEDs that require high voltages. The results obtained in this study clearly show the high potential of stretchable MSC arrays as embedded energy storage devices integrated into stretchable electronics for fabricating body-implanted and wearable devices that can be operated without any wire connection to external power sources.

RESULTS AND DISCUSSION

In order to minimize the strain on the MSCs upon mechanical deformation, the stretchable substrate is designed to consist of two different regions: isolated islands on which the MSCs are attached (islands) and the area between islands (thin film), as shown in Figure 1a. The islands are made of a stiff polymer (PDMS) with high Young's modulus (615 kPa), while the thin film is made of a soft polymer mixture of Ecoflex and PDMS (MEP) with low Young's modulus (122 kPa).

The fabrication steps for the stretchable substrate are illustrated in Figure 1b. First, two pieces of Teflon-coated stainless-steel molds are prepared. Thin iron wires with a diameter of 200 μm are inserted into holes in the bottom mold for fabricating interconnection channels of Galinstan. The wires are fixed to the bottom mold and are then bent using a pair of tweezers. The wires are then fitted into holes in the top mold, and PDMS is poured into the islands of two molds to make rigid islands for attaching MSCs and switch. After half-curing at 65 °C in an oven for 13 min to attach the thin film, both molds are attached and a mixture of Ecoflex and PDMS with a weight ratio of 8:2 is poured into the space for forming a thin film layer between the molds. After the molds are cured at 65 °C in an oven for 90 min, the stretchable substrate is separated and wires are pulled out simultaneously. The fabricated stretchable substrate is composed of island (1 cm × 0.9 cm) arrays and a thin MEP film (thickness 1.8 mm) between the islands with a separation of 0.4 cm. Through the channels made by iron wires, Galinstan is injected using a microsyringe. Galinstan is a liquid eutectic alloy consisting of 68.5% Ga, 21.5% In, and 10% Sn, and its melting temperature is −19 °C.[40] On top of the PDMS islands, MSCs are dry-transferred. For electrical contacts between the MSC and Galinstan interconnections without corrosion of Au electrodes, Ag nanowires dispersed in water are drop-cast.[41]

The simple fabrication processes for the MSCs are shown in Figure 1c. MSCs are fabricated on top of the PET film, which was spin-coated on top of a PDMS/SiO_2 substrate. Owing to poor adhesion between the PET film and PDMS, the MSCs fabricated on the PET film can be easily detached. A total of 16 MSCs are dry-transferred on top of the PDMS islands. The electrodes are fabricated via a 19-LbL assembly of functionalized MWNTs and a top layer of MWNT/Mn_3O_4 composite; MWNT-NH_3^+ and MWNT-COO^- are alternately adsorbed by electrostatic attraction on a gold-patterned collector surface (Figure 1d).[42] After the 19 cycles of LbL assembly, the substrate is dipped into a MWNT-COO^-/Mn_3O_4 solution for 10 min to coat a top layer of the (MWNT-NH_3^+/MWNT-COO^-)$_n$ film.[38] Finally, the PVA-H_3PO_4 electrolyte is drop-cast onto the electrode surface to fabricate all-solid-state MSCs. For confirming LbL deposition, UV−visible absorption spectra are taken and are shown in Figure S1a (Supporting Information). The UV absorbance at 267 nm linearly increases with the number of bilayers on the quartz substrate, confirming the uniform thickness of each
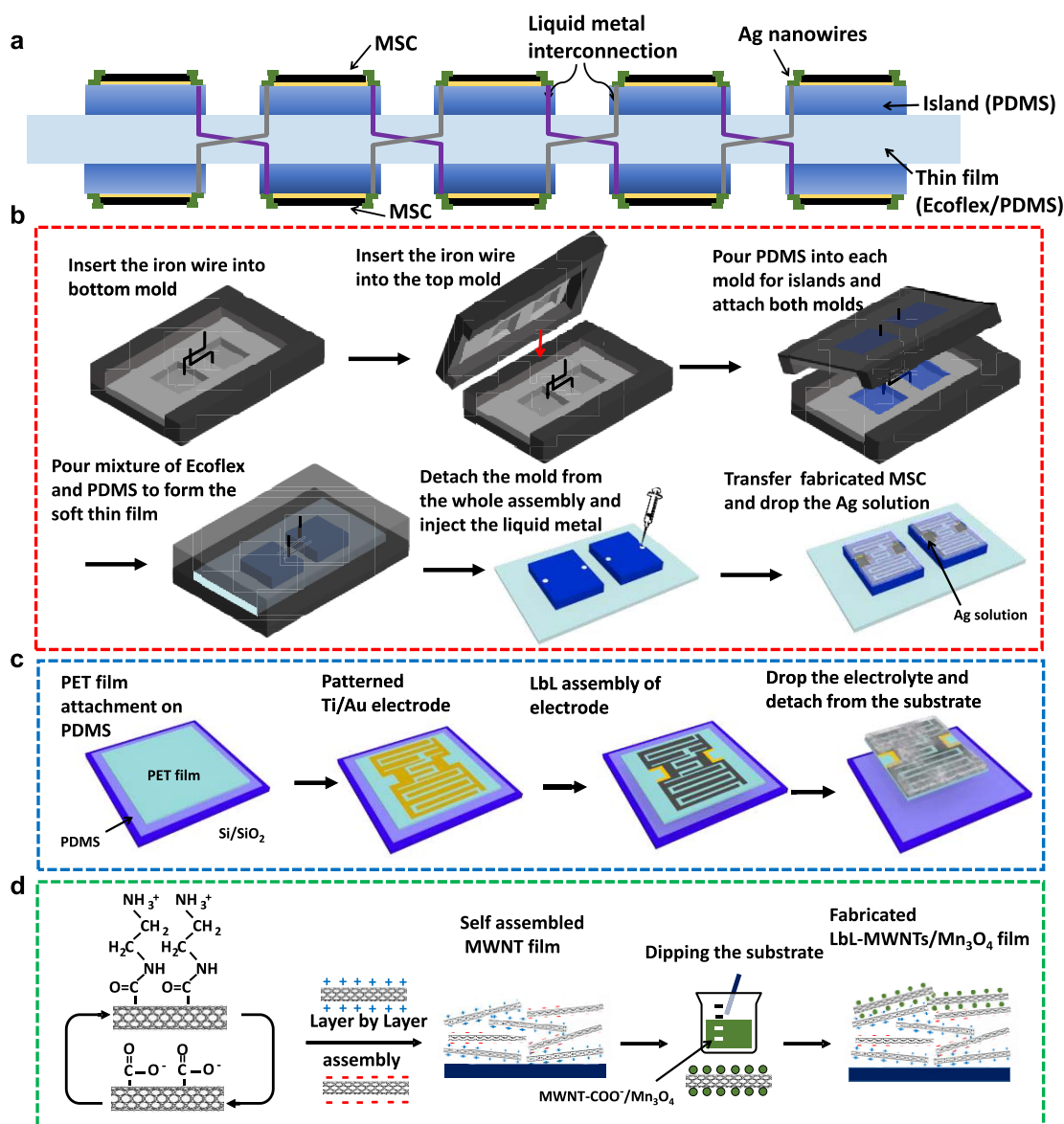
Figure 1. Schematic illustration of fabrication processes for stretchable devices: (a) side view of integrated MSCs on the stretchable substrate; (b) fabrication of stretchable substrate, embedded interconnection, and dry transfer of MSCs; (c) fabrication of MSC on PET film; (d) fabrication of hybrid MWNT film/Mn_3O_4 electrode *via* layer-by-layer assembly.

layer. Figure S1b (Supporting Information) shows an SEM image of the LbL-MWNTs/Mn_3O_4 film consisting of the 19 LbL-MWNTs film and top MWNT-COO$^-$/Mn_3O_4 layer; the inset shows a cross-sectional SEM image indicating a uniform thickness of 220 nm over the large area.

Figure S2 (Supporting Information) shows the X-ray diffraction (XRD) pattern of the MWNT-COOH/Mn_3O_4 powder synthesized in this work, confirming the chemical composition of manganese oxide as Mn_3O_4 with its characteristic diffraction peaks. The diffraction peaks matched well with those of the tetragonal hausmannite phase. The lattice constants were evaluated to be $a = 5.765$ and $c = 9.442$ Å, which are consistent with the standard values for bulk Mn_3O_4 (JCPDS card no. 24-0734).[43] The additional peaks

marked with stars were represented as the (002), (100), and (101) reflections of MWNTs.[44] Furthermore, no clear impurity peaks were obtained, indicating the high purity of Mn_3O_4.

Electrochemical properties of the fabricated MSCs are measured by taking cyclic voltammetry (CV) curves, galvanostatic charge−discharge curves, and electrochemical impedance spectra (EIS). Here, single MSC and array MSC represent only 1 MSC and 16 MSCs, respectively. The arrays of 16 MSCs are composed of 4 MSCs connected in series (4S) and 4 sets of 4S connected in parallel (4P). It is ideally expected that a circuit of 4S + 4P MSCs would have the same total capacitance but 4 times higher output voltage in comparison to a single MSC, under the assumption that the contact resistance is negligible. In order to
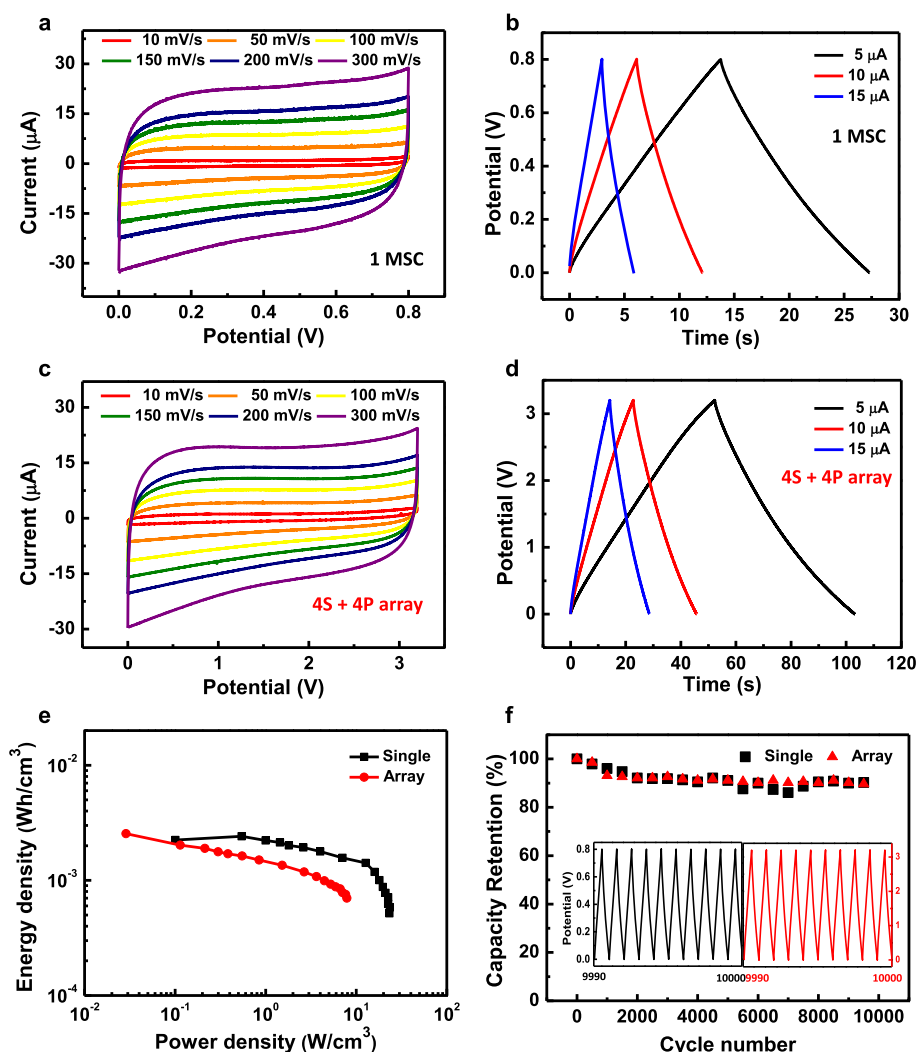
Figure 2. Electrochemical properties of single and array MSCs: (a) CV curves of a single MSC at different scan rates varying from 10 to 300 mV/s; (b) galvanostatic charge−discharge curves of a single MSC at different currents; (c) CV curves of the 4S + 4P array of MSCs at different scan rates varying from 10 to 300 mV/s (the inset circuit shows the 4S + 4P array of MSCs); (d) galvanostatic charge−discharge curves of the 4S + 4P array of MSCs at different current densities; (e) Ragone plots for a single MSC (black) and the 4S + 4P array of MSCs (red); (f) capacity retention of a single MSC (black) and the 4S + 4P array of MSCs (red) as a function of cycling number (the inset shows the charge−discharge curves between 9990 and 10000 cycles).

ensure reproducible electrochemical performance of the fabricated MSCs, the CV curves for 16 MSCs are compared at a scan rate of 300 mV/s in Figure S3 (Supporting Information). It is clearly shown that the 16 MSCs exhibit a similar total capacitance value with variations within 10%. Here, we have used 5 different designs for MSCs depending on the position of the interconnection line on our stretchable substrate, as shown in Figure S4 (Supporting Information): 8 MSCs of type 1 and 2 MSCs of types 2−5 whose interspace and active area are 150 μm and 0.6 cm^2, respectively. The active area includes two LbL-MWNTs/Mn$_3$O$_4$ film electrodes and interspace. MSCs with different designs exhibit almost the same value for total capacitance.

Parts a and c of Figure 2 show the CV curves obtained from the single and array MSCs, respectively. The CV curves of the MSCs are rectangular and symmetric in shape regardless of the scan rate, which

ranged from 10 to 300 mV/s. As expected, the output voltage increases by 4 times in the case of the 4S connection of MSCs. The total capacitance can be calculated using the equation $C = (2 \times \oint I \, dV)/(S \times \Delta V)$, where I is the measured current, ΔV is the operation voltage window, and S is the scan rate. Using this equation, the total capacitances for the single and array MSCs are calculated to be 378 and 343 μF, respectively, at a scan rate of 10 mV/s, as shown in Figure 2c. The slightly lower capacitance of the array MSC in comparison to that of the single MSC is probably due to the increased number of contact resistance points between interconnection lines for the 4S + 4P circuit construction.

Galvanostatic charge−discharge measurements for the single and array MSCs have been carried out at various currents, as shown in parts b and d of Figure 2, respectively. Regardless of the current applied, all of

the charge−discharge curves show ideally symmetric triangular shapes, confirming a high Coulombic efficiency of ∼100%. The discharging time for the array MSC is about 4 times longer than that for the single MSC, as is expected from the circuit design of the parallel connection of 4S MSCs.

Furthermore, the excellent performance of our MSC array is shown in a Ragone plot (Figure 2e). The total volume of the MSC is estimated to be 13.2 cm^3, where the thickness of the electrode is 220 nm. The specific energy (E_{cell}) and power (P_{cell}) densities of a cell are estimated from the CV curves by using the relationships $E_{cell} = C_{cell} \times (\Delta V)^2/7200$ and $P_{cell} = E_{cell} \times 3600/\Delta t$, where C_{cell} is volumetric capacitance, ΔV is the operating voltage range, and Δt is the discharging time. The single and array MSCs exhibit maximum volumetric energy densities of 2.6 and 2.4 mWh/cm^3, respectively, and maximum volumetric power densities of 23 and 8 W/cm^3, respectively. In addition, the areal capacitance for the single and array MSCs are calculated to be 0.63 and 0.57 mF/cm^2, respectively. These values are smaller than those obtained from the MSCs with vertically aligned MWNT/metal oxide electrodes in liquid electrolyte.[45,46] The use of aligned MWNTs would result in superior ion diffusivity, since they have a regular pore structure and large pore sizes in comparison to the film of randomly oriented MWNTs.[47] The typical Nyquist plots for single and array MSCs are shown in Figure S5 (Supporting Information). At low frequencies, the imaginary part of the impedance sharply increases and the plot tends to be a vertical line characteristic of capacitive behavior.[48] In the middle range of frequencies, the influence of the porosity and thickness of the electrode on the migration rate of ions from the electrolyte to deep inside the electrode is observed. The equivalent series resistances (ESRs) of the single and array MSCs are measured to have values of 155 and 197 Ω, respectively. Due to the contact resistance between the interconnection line and MSCs, the array MSC has a slightly higher ESR value and the curve is not vertical along the imaginary y axis in comparison to that of the single MSC. The inset of Figure S5 shows the evolution of the imaginary part of the normalized capacitance (C'') vs frequency for single and array MSCs. A fast frequency response of single and array MSCs is confirmed by a short relaxation time constant (τ_0). τ_0 is the transition point of the electrochemical capacitor from capacitive to resistive behavior and corresponds to the point of maximum energy dissipation.[49] The capacitor response frequencies (f_0) of single and array MSCs are about 1.87 and 0.534 Hz, respectively. Therefore, τ_0 is calculated to be 0.53 and 1.87 s, respectively, by the equation $\tau_0 = 1/f_0$. The array MSC exhibits a rather long response time due to many contact points between the interconnection and MSC, which should be improved later.

Figure 2f shows the capacitance retention of single and array MSCs during repetitive charge−discharge cycles. About 90% of the initial capacitance value of the single MSC is maintained after 10000 charge−discharge cycles, and 89% of the initial capacitance value of the array MSC is maintained after 10000 repetition cycles. The inset of Figure 2f shows the typical charge−discharge curves between 9990 and 10000 cycles without any deterioration, satisfying the requirement of long cycle life.

Strain distribution on the stretchable substrate with strain applied on it is calculated by using the finite element method (FEM). The array of islands and thin film between the islands are modeled using a commercial finite element program, ABAQUS.[50] The initial shear modulus and bulk modulus of PDMS are taken as 2 and 200 MPa, respectively, and the values for the MEP thin film are taken as 0.4 and 40 MPa, respectively. The initial shear modulus and bulk modulus of the thin film can be calculated as $G_{mix} = G_{PDMS}f_{PDMS} + G_{Ecoflex}f_{Ecoflex}$, where G is the initial shear modulus, the values of which are 615 and 9.542 kPa for PDMS and Ecoflex, respectively, and f is the volume fraction, the values of which are 0.8 and 0.2 for Ecoflex and PDMS, respectively. The neo-Hookean constitutive models are used for the materials.[51,52] The strain applied on the islands can be suppressed more by positioning a PET film on top of the islands, owing to the much higher Young's modulus of the PET film (3.1 GPa) in comparison to that of PDMS (615 kPa). The strain distribution under 40% uniaxial strain is schematically shown in Figure 3a. As was intended with our design of the deformable substrate, the islands with PET films hardly deform; moreover, the deformation is concentrated on the MEP thin film between two neighboring islands. This tendency can be also shown from a different view, a side view of the A-A′ section. The substrate is stretched gradually until the nominal strain of the unit module reaches 40%. The unit module is defined as shown in Figure 3b, and the nominal strain is defined as $\varepsilon_{applied} = (l' - l)/l$, where l' and l are the lengths of the unit module after and before the deformation, respectively. The original and deformed shapes of the unit module are shown in Figure 3c. Because the modulus of the island with PET film is much higher than that of the substrate, the strain of the island is only 7% obtained from the optical image, while the MEP thin film between two neighboring islands is as high as 120%, as the nominal strain of the unit module is 40%. Because of kinematic compatibility, the strain on the island must be equal to that on the substrate at the interface where the islands are mounted. Therefore, the large strain at the interface is quickly decreased to a small value at the surface. The strain contour by a result of finite element analysis is similar to that from the optical image, as shown in this figure.

Figure 4a shows a photograph of the stretchable substrate with integrated MSC arrays, a switch, and an LED under an applied strain of 40%; the corresponding image of strain distribution is shown in Figure 4b.
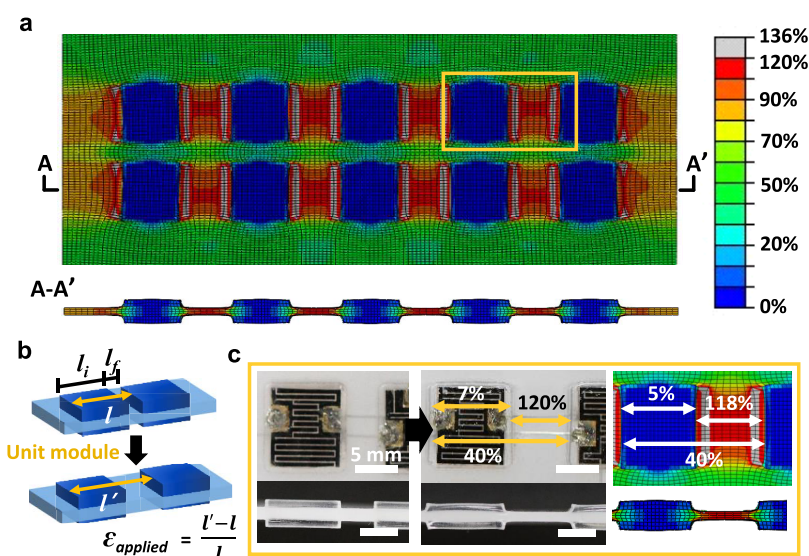
Figure 3. FEM analysis results for strain distribution on the stretchable substrate under a uniaxial strain of 40% with corresponding color scales of strain: (a) (top) strain in a two-dimensional plane and (bottom) strain in the A-A′ cross-section; (b) definition of applied strain ($\varepsilon_{applied}$) on the stretchable substrate; (c) optical images of the stretchable MSC array on deformable substrate under the strain of 0% (left) and 40% (middle) and the corresponding strain distribution under applied strain of 40% (right).

As expected from the previously conducted FEM analysis of strain distribution for our stretchable substrate (Figure 3), the islands with PET films hardly deform and the deformation is concentrated on the MEP thin film between two neighboring islands. CV curves taken from the array MSC at a scan rate of 200 mV/s with varying uniaxial strain of up to 40% are shown in Figure 4c. CV curves were obtained for both directions of stretching and releasing. During the cycles of stretching and releasing, no noticeable damage or defect was observed in the entire device, including the MSCs and embedded Galinstan interconnection, confirming the mechanical stability of our stretchable array of MSCs. Figure 4d shows changes in the normalized capacitance (C/C_0) estimated from the CV curves shown in Figure 4c with varying applied strain, where C and C_0 are the capacitances after and before strain application, respectively. In both deformation directions, *i.e.*, stretching (black) and releasing (red), the normalized capacitance of the array MSC remains constant, indicating mechanically stable device performance up to a uniaxial stretching of 40%. In ambient air conditions, the electrochemical performance of the MSC array is measured while the substrate is stretched repeatedly with an applied strain of 40%. In Figure 4e, CV curves taken after repeated stretching of the whole device are shown. The CV curve maintains a rectangular shape even after 3000 repetitions of stretching under 40% uniaxial strain. The normalized capacitances (C/C_0) estimated from the CV curves are shown in Figure 4f. After 3000 repetitions of stretching under 40% strain, the capacitance seems to decrease by 8%. Such a slight decrease could be attributed to the combined effects of mechanical deterioration due to

repeated stretching and degradation of the polymer electrolyte in ambient air. In our separate experiment on the aging of MSC performance in ambient air, it was found that the normalized capacitance of an MSC degraded with time by 5% after 4.5 h (Figure S6 (Supporting Information)). In this study, it took about 4.5 h to repeat the stretching 3000 times. Therefore, the slight decrease observed in Figure 4f seems to have originated from the degradation of the polymer electrolyte in ambient air rather than from the mechanical weakness of our stretchable MSC array.[53]

The chemical safety of the wearable devices is another important issue. In particular, phosphoric acid is used as the electrolyte in our MSC. As a preliminary experiment, the electrochemical performance of the MSC was measured after the encapsulation of the MSC and compared with that of MSC without encapsulation. Half-cured thin PDMS film was attached on the MSC, and the whole device was fully cured in air for 24 h, as shown in Figure S7a (Supporting Information). The MSC with PDMS encapsulation exhibits no noticeable change in the CV curves even under strain of 40%, as shown in Figure S7b (Supporting Information). Furthermore, the CV curve obtained from the MSC wrapped around the wrist after encapsulation did not show any difference. These results suggest the successful performance of our stretchable MSC arrays with encapsulation, which would be applied to future wearable devices.

Figure 5 also shows that MSC arrays integrated onto the deformable substrate exhibit stable performance under bending and twisting. A photograph of the array MSC on the deformable substrate bent over a bar with a radius of 2 cm and the corresponding color picture of
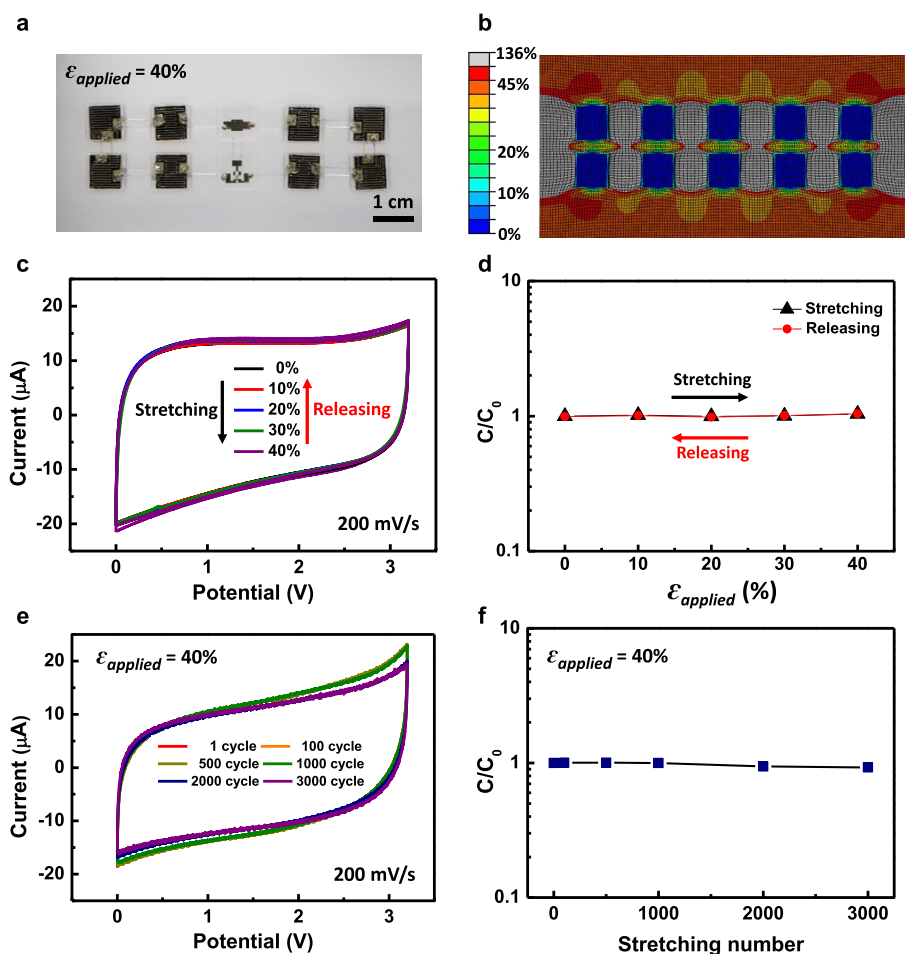
Figure 4. (a) Photograph of MSC array under an applied strain of 40%. (b) Distribution of maximum principal strain estimated using the finite element method (FEM) upon uniaxial stretching at an applied strain of 40%. (c) CV curves of the MSC array obtained while increasing the strain from 0% to 40% (stretching) and decreasing the strain from 40% to 0% (releasing). (d) Normalized capacitance (C/C_0) of MSC array with strain varying between 0% and 40%: black triangles (stretching) and red circles (releasing). (e) CV curves of MSC array subjected to repeated stretching under an applied strain of 40%. (f) Normalized capacitance (C/C_0) as a function of number of stretching cycles under a strain of 40%. C and C_0 are the capacitances after and before stretching, respectively.

the strain distribution obtained by FEM analysis are shown in Figure 5a. The assembly of the islands and substrate subjected to pure bending is simulated using a finite element model. The radius of the curvature is 2 cm. Again, because of the stiff islands, the MEP film between two adjacent islands is deformed more. The strain on the surface of the islands is only 0.01%. The corresponding photograph and strain distribution when the device array is twisted by 180° are also shown in Figure 5b. The twisting looks severe, but the strains on both islands and the MEP film substrate are very small. This is because the surface of the twisted assembly is bilinear, in which the longitudinal and transverse strains are very small. The FEM analyses for bending and twisting clearly show that the islands on which the MSCs are mounted hardly deform and the surface of the islands and PET film remain flat after the whole device array is deformed. Such behavior of minimizing the strain on islands is identical with that observed during stretching (Figure 4). In comparison to

stretching, bending and twisting do not apply high strain even on the thin film area.

CV curves at a scan rate of 200 mV/s and the normalized capacitance of array MSCs on the stretchable substrate under bending and twisting are shown in parts c and d of Figure 5, respectively. Bending of the array MSCs on the stretchable substrate with various bending radii down to 2 cm does not induce any deterioration in the electrochemical performance. Moreover, the twisting of the array MSCs by 90, 180, and 270° does not degrade their electrochemical performance. As can be clearly observed, the performance of MSCs remains the same regardless of the deformation, demonstrating the mechanical stability of the array MSCs fabricated on our stretchable substrate.

Since our planar-type MSCs can be integrated on both sides of the stretchable substrate, the density of MSCs per substrate is expected to be higher than that of MSCs integrated on a conventional planar substrate with the same surface area. In order to confirm this
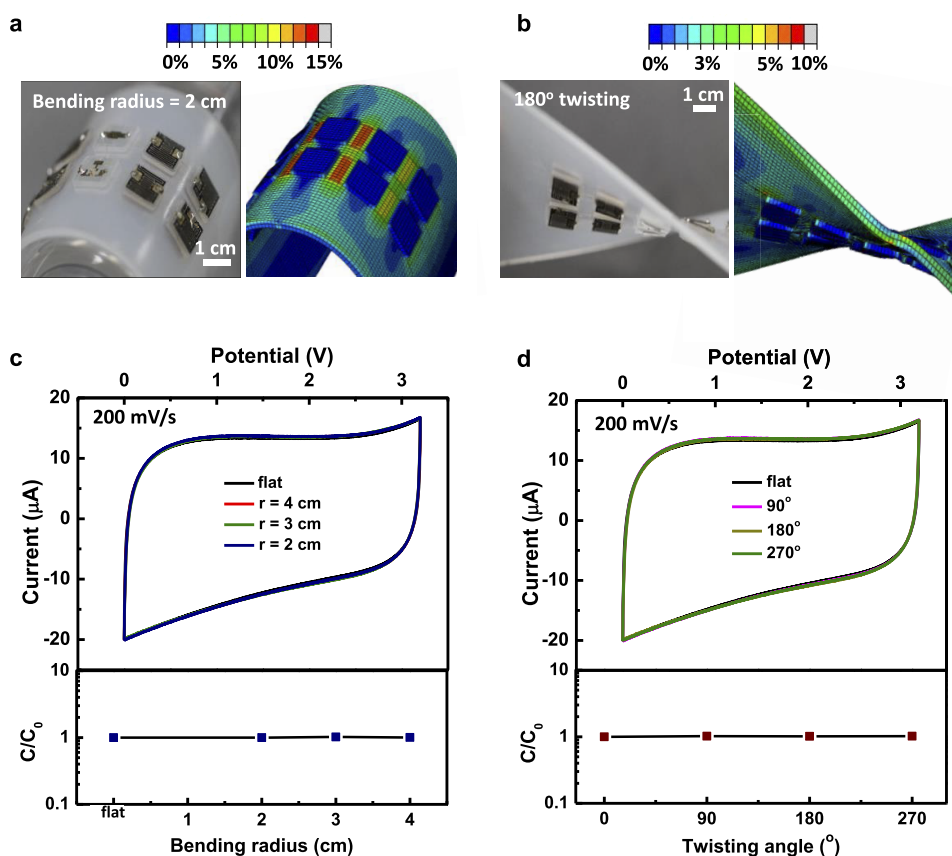
Figure 5. (a, b) Optical images of the stretchable substrate and the distribution of maximum principal strain estimated using FEM upon various deformations: (a) bending with a bending radius of 2 cm; (b) twisting by 180° over a length of 6.1 cm. The film on top of the islands is composed of MSCs, switch, and LED on a PET film. (c, d) CV curves and normalized capacitance of MSCs array under (c) bending and (d) twisting.

expectation, the device performances of integrated MSCs on our stretchable substrate and those on a conventional planar substrate are compared. For simplicity, the electrodes are fabricated *via* spray coating of MWNTs on patterned Ti/Au electrodes. The structures of these two substrates are shown in Figure 6a. The dimensions of both the substrates in the two-dimensional plane are identical, and embedded Galinstan interconnections are used in both substrates, as shown in the schematic. The only difference is that MSCs can be integrated on both sides of our stretchable substrate, while in the case of the conventional planar substrate, MSCs can be integrated only on the top surface. Consequently, a total of three and six MSCs can be integrated on the conventional planar substrate and our stretchable substrate, respectively. CV curves obtained at a scan rate of 100 mV/s from the two MSC arrays with varying uniaxial strain of up to 30% are shown in Figure 6b. As expected, the MSCs on the stretchable substrate (simply named as 3D substrate) (blue) show higher current than that shown by the MSCs on the planar one (red), regardless of the applied strain. For all MSC arrays, the CV curves do not show any noticeable change with uniaxial stretching, confirming the mechanically sturdy structures of both

substrates, including the embedded Galinstan interconnection. The total capacitances of the MSC array attached on both sides of our stretchable substrate and of the conventional planar substrate are 209 and 98 μF, respectively. As expected, the total capacitance is doubled upon the integration of MSCs on the stretchable substrate. Charge−discharge curves taken from the MSCs on the planar and stretchable substrates are shown in Figure 6c. The discharge time for the MSC array on our stretchable substrate is estimated to be twice that for the MSC array on the planar substrate, again suggesting that the capacitance doubled in the case of double-sided integration of MSCs.

Normalized capacitance (C/C_0, where C and C_0 denote capacitance after and before strain application, respectively) is estimated at varying applied strain for both MSC arrays, and the results are shown in Figure 6d. Upon application of 30% strain, slight decreases of 0.4% and 8% in the capacitance are observed for the MSCs on the planar substrate and our stretchable substrate, respectively. This slight decrease can also be attributed to the collective contribution from poor contacts between MSCs and Galinstan interconnections and the degradation of the polymer electrolyte in ambient air.
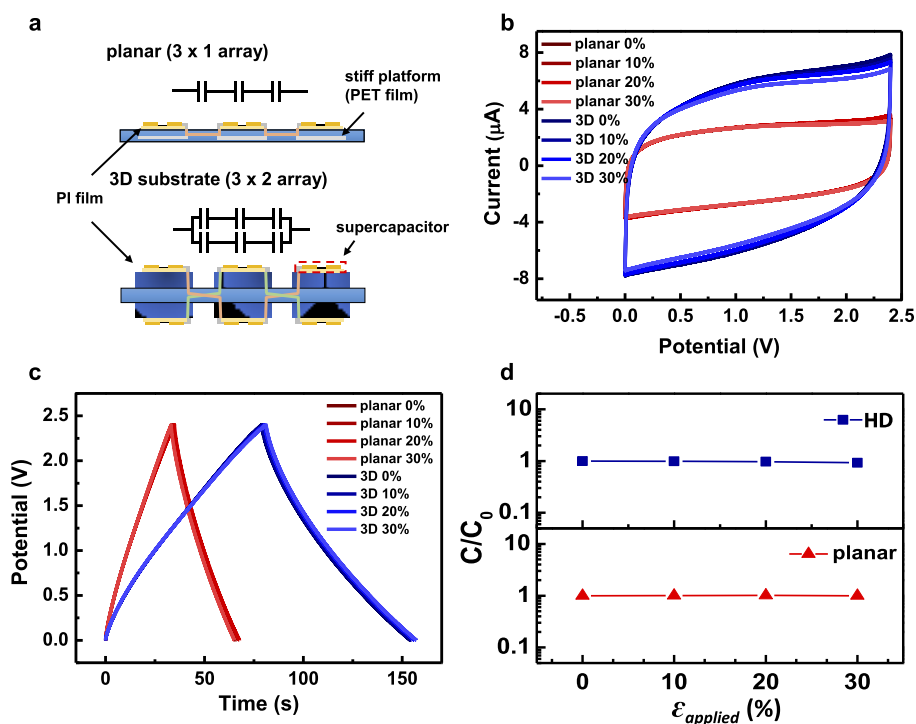
Figure 6. (a) Schematic diagrams of three MSCs connected in series on a planar substrate and two sets of three serially connected MSCs attached on both sides of our stretchable substrate. Here, our deformable substrate is named 3D substrate for simplicity. (b) CV curves of array MSC on planar (red) and 3D (blue) substrate with varying applied strain. (c) Charge– discharge curves of MSCs on planar (red) and 3D (blue) substrates at various applied strains. (d) Normalized capacitance (C/C_0) for MSCs on 3D (top, blue) and on planar (bottom, red) substrates. Here, C and C_0 are the capacitances after and before strain application, respectively.
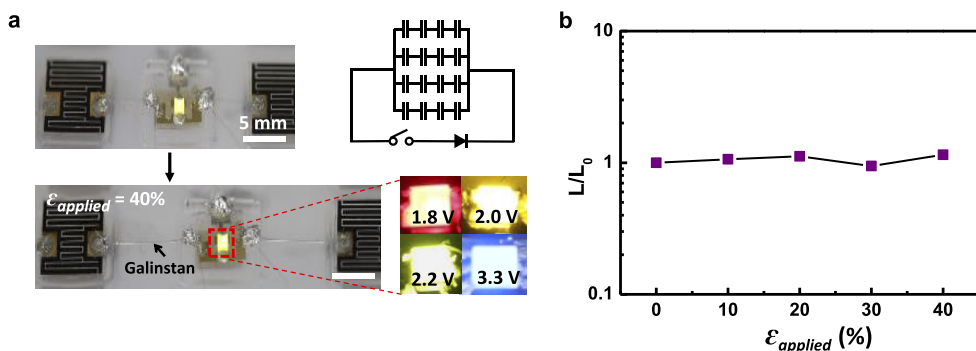

Figure 7. (a) Optical images of MSC array and LED on the stretchable substrate before (top left) and after (bottom left) application of 40% strain. The circuit diagram is shown schematically (top right). Various LEDs operating at different bias voltages are lit by a circuit of multiple MSCs (bottom right): red (1.8 V), yellow (2.0 V), green (2.2 V), and blue (3.3 V). (b) Normalized brightness of LEDs with radiation under a uniaxial strain of up to 40%. L and L_0 are the brightnesses after and before application of 40% strain, respectively.

Furthermore, the use of embedded Galinstan interconnections increases fill factors to be more than those in the case of serpentine suspended interconnections adopted in our previous study on the fabrication of a stretchable MSC array.[39] The fill factor is defined by the relation fill factor = (active area of MSCs)/(total area), where total area includes the active area of MSCs and interconnections, as shown in Figure S8 (Supporting Information). Due to the space required for the suspended serpentine interconnections, the fill factor of the MSCs in our previous study was 13.6% for the total area (blue dotted area, 34.22 cm^2) and active area of

MSCs (red dotted area, 0.12 cm^2 × 4), while that of the MSCs on a planar substrate with embedded interconnections is 39% for the total area (blue dotted area, 6.24 cm^2) and active area of MSCs (red dotted area, 0.6 cm^2 × 4). The integration of MSCs on both sides of the deformable substrate in this study further increased the fill factor to 78%.

For realizing wearable or bioimplantable devices that do not require any external power source, active devices need to be operated using energy storage devices. One of the advantages of array MSCs is that the output voltage can be adjusted by integrating

them into a circuit. In this study, after array MSCs are charged with the switch in the "OFF" position, an LED is lit using the MSCs with the switch in the "ON" position. By integration of MSCs in a serial connection, output voltage higher than that normally obtained using the PVA-H$_3$PO$_4$ electrolyte (0.8 V) can be achieved. As a result, various μ-LEDs with different operating voltages could be lit: red (1.8 V), yellow (2.0 V), green (2.2 V), and blue (3.3 V) LEDs, as shown in Figure 7a. At an applied uniaxial strain of 40%, the μ-LED remains brightly lit. While the uniaxial strain is increased, the brightness of the μ-LED is measured in a dark room. For measurement of the brightness of the μ-LED, the array MSCs on our stretchable substrate are fixed on a homemade stretching stage and an illuminometer is placed at a distance of 3 cm from the stage. The corresponding circuit diagram is also shown. The normalized brightness of the μ-LED (L/L_0; where L_0 and L are the brightness of the μ-LED before and after strain application, respectively) is measured at varying applied strain, and the results are shown in Figure 7b. It is shown that nearly constant brightness of the μ-LED is observed under an applied strain of up to 40%, demonstrating the mechanical stability of the whole integrated circuit of array MSCs, switch, and μ-LED on our stretchable substrate.

CONCLUSIONS

In this paper, we report the successful fabrication of stretchable microsupercapacitor arrays on a deformable polymer substrate that exhibits high electrochemical performance even under mechanical deformation such as bending, twisting, and uniaxial strain of up to 40%. Our deformable substrate is designed to minimize the strain on active devices by adopting a heterogeneous structure consisting of stiff PDMS islands (for attaching active devices) and a soft thin film (prepared from a mixture of Ecoflex and PDMS) between neighboring PDMS islands. FEM analysis of strain distribution reveals that almost no strain exists on the PDMS islands but concentrated strain is present on the soft thin film area. The liquid metal Galinstan is used as an embedded interconnection, thereby simplifying the fabrication as well as providing mechanical stability even under high external strain. Furthermore, the double-sided integration of MSCs increases the capacitance to twice that obtained using a conventional planar deformable substrate. Planar-type MSCs with LbL-assembled hybrid thin film electrodes of MWNT/Mn$_3$O$_4$ and PVA-H$_3$PO$_4$ electrolyte have been fabricated in this study. When they are integrated into a circuit, these MSCs provide output voltage beyond the potential of the electrolyte used. Thus, these MSCs can be used to operate various LEDs that require high voltages. The results obtained in this study demonstrate the high potential of our stretchable MSC arrays for their application as embedded stretchable energy storage devices in bioimplantable and future wearable nanoelectronics.

METHODS

Fabrication of Stretchable Substrate. Two pieces of Teflon-coated stainless-steel molds were used as the top and bottom molds for the fabrication of our deformable substrates with polymer materials. First, Fe wires with a length of 15 cm and a diameter of 200 μm were inserted into holes in the bottom mold, which was used to construct the channels of the Galinstan (Rotometals) interconnection. Second, these wires were fitted into holes in the other mold. PDMS (Sylgard 184, Dow Corning) was poured into the trench areas of both molds to form isolated rigid islands for attaching active devices. Third, PDMS in the two molds was annealed in an oven at 65 °C for 13 min for half-curing. The annealed PDMS functioned as a bonding island for the thin film prepared from a mixture of Ecoflex (Ecoflex 0030, Smooth-On) and PDMS (MEP film). After half-curing, both molds were combined. Fourth, the MEP film with a weight mixing ratio of 8:2 was poured through a space between the molds to form a thin film layer. After the entire mold was cured in a dry oven at 65 °C for 90 min, the deformable substrate was carefully disjoined from the mold, and Fe wires were simultaneously eliminated. The mixing ratios of Ecoflex and PDMS and the relative size of the PDMS island to the separation of the islands were optimized according to the desired stretchability and areal densities of the active devices.

Fabrication of Patterned All-Solid-State Microsupercapacitor. After spin-coating of PDMS at 2000 rpm for 30 s onto a Si/SiO$_2$ substrate, it was cured at 100 °C for 10 min. On the PDMS film, a PET film (75 μm) was attached. To form a current collector and pads for electrical measurements, a Ti/Au (5/50 nm) film deposited on the PET film by e-beam evaporation was patterned by photolithography. Then, a functionalized MWNT film was coated on the patterned Ti/Au electrodes *via* LbL assembly: dried MWNT-COOH and MWNT-NH$_2$ powders were dispersed in DI water by using sonication to form a stable dispersion. The concentration of both solutions was 1 mg/mL, and the pH values of the solutions were 3.6 and 6.4, respectively. The patterned substrate was dipped in a MWNT-NH$_2$ solution for 10 min and was washed with deionized water (DI water) for 1 min to remove weakly absorbed MWNTs. The substrate was then submerged in a MWNT-COOH solution for 10 min and washed with DI water for 1 min. After this cycle was repeated 19 times, the substrate was dipped in a MWNT-COOH/Mn$_3$O$_4$ solution for 10 min. The residual LbL-assembled MWNT/Mn$_3$O$_4$ film except for the patterned area was removed *via* the lift-off process. Finally, the PVA-H$_3$PO$_4$ gel electrolyte was drop-cast onto the electrode surface.

Functionalization of Negatively and Positively Charged MWNTs. MWNTs (Aldrich, purity >95%, length 5 μm, outer diameter 6−9 nm) were refluxed in concentrated sulfuric acid and nitric acid (3/1 v/v, Sigma-Aldrich) at 70 °C for 3 h to prepare carboxylic acid functionalized MWNTs (MWNT-COOH). These functionalized MWNTs were rinsed with DI water several times using a cellulose ester membrane filter (ADVANTEC MFS, Inc.; pore size 0.2 μm, diameter 47 mm). After osmosis filtration carried out using a tube cellulose membrane (Sigma; average flat width 33 mm, average diameter 21 mm), MWNT-COOH was finally obtained.

Amine-functionalized MWNTs (MWNT-NH$_2$) were obtained by combining a mixture of NH$_2$(CH$_2$)$_2$NH$_2$ (Sigma-Aldrich) and 1-ethyl-3-(3-(dimethylamino)propyl)carbodiimide (EDC, Aldrich) with an aqueous solution of MWNT-COOH with stirring at room temperature for 5 h.

Synthesis of MWNT-COOH/Mn$_3$O$_4$ Nanocomposites. MWNT-COOH/Mn$_3$O$_4$ nanocomposites were synthesized by the hydrothermal method. A 30 mL portion of ethanol containing 100 mg of Mn(CH$_3$COO)$_2$·4H$_2$O (Aldrich) and dispersed MWNTs were put together in a high-pressure stainless-steel autoclave. The autoclave

was put in an oven at 150 °C for 3 h. After the mixture was cooled to room temperature within 1 day, a black precipitate was obtained and was rinsed with DI water several times using a mixed cellulose ester membrane filter. Thereafter, the filtered composites were dried and peeled off from the membrane filter to obtain MWNT-COOH/Mn_3O_4. Synthesized MWNT-COOH/Mn_3O_4 was investigated by X-ray diffraction (XRD) to confirm the oxidation state of Mn.

Synthesis of PVA-H_3PO_4 Gel Electrolyte. For the preparation of the gel electrolyte, 15 mL of phosphoric acid (H_3PO_4, Sigma) was dropped into 150 mL of DI water, and then 15 g of poly(vinyl alcohol) (PVA, Aldrich, MW 89000–96000) was added. The solution was mixed at 150 °C with vigorous stirring until it became clear.

Transfer of MSC Arrays onto Stretchable Substrate. For the assembly of MSCs on the stretchable substrate, MSCs fabricated on the PET film were dry-transferred. In this way, the fabrication of the substrate can be carried out independently of the MSCs. As a result, conventional electronics on a rigid substrate can be easily integrated on a stretchable substrate.

Electrical Connection between MSCs and Embedded Liquid Metal Interconnections. For connecting MSCs on islands, Galinstan was injected using a commercial syringe in the channel (diameter 200 μm) formed using Fe wires. Galinstan is highly conductive and is in the liquid state at room temperature. A commercially available syringe and needle were used to inject Galinstan into the channel. The injected Galinstan stayed stable inside the channel by forming an oxide film, where it was exposed to air. Electrical contacts between the MSC and embedded Galinstan interconnections are made by drop-casting the Ag nanowires dispersed in water (Dittotechnology, 1 wt % diluted in water). The diameter and average length of Ag nanowires are 2–30 nm and 10 μm, respectively.

Characterization. The chemical composition of the MWNT-COOH/Mn_3O_4 nanocomposite was determined by XRD (Rigaku SmartLab). The structure and morphology of the electrode film were investigated using scanning electron microscopy (SEM, Hitachi S-4800). Photographs of the samples were obtained using a Canon EOS 7D camera. The electrochemical properties of the MSCs were determined by measuring the CV curves and EIS, using an electrochemical analyzer (Ivium Technologies, Compact Stat.). The EIS was investigated in the frequency range from 1 to 10 MHz with a potential amplitude of 10 mV. The brightness of the μ-LED was measured using an illuminometer (TES 1330A, TES). The mechanical stability of the fabricated stretchable MSC arrays was measured using a home-made stretching stage and repetition test machine.

Conflict of Interest: The authors declare no competing financial interest.

Supporting Information Available: Figures giving (1) UV–visible absorption spectra and SEM images of LbL-assembled MWNT thin film, (2) XRD spectrum of MWNT-COOH/Mn_3O_4 nanocomposites, (3) CV curves of 16 different fabricated MSCs, (4) total capacitance of five differently designed MSCs, (5) Nyquist plots for both single and array MSCs, (6) normalized capacitance of MSCs in ambient air, (7) measurement of MSC after encapsulation with PDMS, and (8) optical images of MSC arrays in our previous study and our deformable substrate. This material is available free of charge *via* the Internet at http://pubs.acs.org.

REFERENCES AND NOTES

1. Rogers, J. A.; Someya, T.; Huang, Y. Materials and Mechanics for Stretchable Electronics. *Science* **2010**, *327*, 1603–1607.
2. Kim, D.-H.; Lu, R.; Ghaffari, R.; Kim, Y.-S.; Lee, S. P.; Xu, L.; Wu, J.; Kim, R.-H.; Song, J.; Liu, Z.; *et al.* Materials for Multifunctional Balloon Catheters with Capabilities in Cardiac Electrophysiological Mapping and Ablation Therapy. *Nat. Mater.* **2011**, *10*, 316–323.
3. Hu, L.; Cui, Y. Energy and Environmental Nanotechnology in Conductive Paper and Textiles. *Energy Environ. Sci.* **2012**, *5*, 6423–6435.
4. Kim, R.-H.; Bae, M.-H.; Kim, D. G.; Cheng, H.; Kim, B. H.; Kim, D.-H.; Li, M.; Wu, J.; Du, F.; Kim, H.-S.; *et al.* Stretchable, Transparent Graphene Interconnects for Arrays of Microscale Inorganic Light Emitting Diodes on Rubber Substrates. *Nano Lett.* **2011**, *11*, 3881–3886.
5. Lee, S.-K.; Kim, B. J.; Jang, H.; Yoon, S. C.; Lee, C.; Hong, B. H.; Rogers, J. A.; Cho, J. H.; Ahn, J.-H. Stretchable Graphene Transistors with Printed Dielectrics and Gate Electrodes. *Nano Lett.* **2011**, *11*, 4342–4646.
6. Lee, J.; Wu, J.; Shi, M.; Yoon, J.; Park, S.-I.; Li, M.; Liu, Z.; Huang, J.; Rogers, J. A. Stretchable GaAs Photovoltaics with Designs That Enable High Areal Coverage. *Adv. Mater.* **2011**, *23*, 986–991.
7. Lee, J.; Wu, J.; Ryu, J. H.; Liu, Z.; Meitl, M.; Zhang, Y.-W.; Huang, Y.; Rogers, J. A. Stretchable Semiconductor Technologies with High Areal Coverages and Strain-Limiting Behavior: Demonstration in High-Efficiency Dual-Junction GaInP/GaAs Photovoltaics. *Small* **2012**, *8*, 1851–1586.
8. Jeong, J.-W.; Yeo, W.-H.; Akhtar, A.; Norton, J. J. S.; Li, S.; Jung, S.-Y.; Su, Y.; Lee, W.; Xia, J.; Cheng, H.; *et al.* Materials and Optimized Designs for Human-Machine Interfaces *via* Epidermal Electronics. *Adv. Mater.* **2013**, *25*, 6839–6846.
9. Kettlgruber, G.; Kaltenbrunner, M.; Siket, C. M.; Moser, R.; Graz, I. M.; Schwodiauer, R.; Bauer, S. Intrinsically Stretchable and Rechargeable Batteries for Self-Powered Stretchable Electronics. *J. Mater. Chem.* **2013**, *1*, 5505–5508.
10. Woo, S.-J.; Kong, J.-H.; Kim, D.-G.; Kim, J.-M. A Thin All-Elastomeric Capacitive Pressure Sensor Array Based on Micro-Contact Printed Elastic Conductors. *J. Mater. Chem.* **2014**, *2*, 4415–4422.
11. Kim, D.-H.; Song, J.; Choi, W. M.; Kim, H.-S.; Kim, R.-H.; Liu, Z.; Huange, Y. Y.; Hwang, K.-C.; Zhang, Y.-W.; Rogers, J. A. Materials and Noncoplanar Mesh Designs for Integrated Circuits with Linear Elastic Responses to Extreme Mechanical Deformations. *Proc. Natl. Acad. Sci. U.S.A.* **2008**, *105*, 18675–18680.
12. Aricò, A. S.; Bruce, P.; Scrosati, B.; Tarascon, J.-M.; Van Schalkwijk, W. Nanostructured Materials for Advanced Energy Conversion and Storage Devices. *Nat. Mater.* **2005**, *4*, 366–377.
13. Wang, X.; Liu, B.; Wang, Q.; Song, W.; Hou, X.; Chen, D.; Cheng, Y.-B.; Shen, G. Three-Dimensional Hierarchical $GeSe_2$ Nanostructures for High Performance Flexible All-Solid-State Supercapacitors. *Adv. Mater.* **2013**, *25*, 1479–1486.
14. Winter, M.; Brodd, R. J. What are Batteries, Fuel Cells, and Supercapacitors? *Chem. Rev.* **2004**, *104*, 4245–4270.
15. Fan, Z.; Yan, J.; Zhi, L.; Zhang, Q.; Wei, T.; Feng, J.; Zhang, M.; Qian, W.; Wei, F. A Three-Dimensional Carbon Nanotube/Graphene Sandwich and Its Application as Electrode in Supercapacitors. *Adv. Mater.* **2010**, *22*, 3723–3728.
16. Simon, P.; Gogotsi, Y. Materials for Electrochemical Capacitors. *Nat. Mater.* **2008**, *7*, 845–854.
17. Chu, A.; Braatz, P. Comparison of Commercial Supercapacitors and High-Power Lithium-Ion Batteries for Power-Assist Applications in Hybrid Electric Vehicles I. Initial Characterization. *J. Power Sources* **2002**, *112*, 236–246.
18. Wang, H.; Liang, Y.; Mirfakhrai, T.; Chen, Z.; Casalongue, H. S.; Dai, H. Advanced Asymmetrical Supercapacitors Based on Graphene Hybrid Materials. *Nano Res.* **2011**, *4*, 729–736.
19. Arbizzani, C.; Biso, M.; Cericola, D.; Lazzari, M.; Soavi, F.; Mastragostino, M. Safe, High-Energy Supercapacitors Based on Solvent-Free Ionic Liquid Electrolytes. *J. Power Sources* **2008**, *185*, 1575–1579.
20. Yu, C.; Masarapu, C.; Rong, J.; Wei, B.; Jiang, H. Stretchable Supercapacitors Based on Buckled Single-Walled Carbon Nanotube Macrofilms. *Adv. Mater.* **2009**, *21*, 4793–4797.
21. Jiang, H.; Khang, D.-Y.; Song, J.; Sun, Y.; Huang, Y.; Rogers, J. A. Finite Deformation Mechanics in Buckled Thin Films on Compliant Supports. *Proc. Natl. Acad. Sci. U.S.A.* **2007**, *104*, 15607–15612.

22. Xu, P.; Gu, T.; Cao, Z.; Wei, B.; Yu, J.; Li, F.; Byun, J.-H.; Lu, W.; Li, Q.; Chou, T.-W. Carbon Nanotube Fiber Based Stretchable Wire-Shaped Supercapacitors. *Adv. Mater.* **2014**, *4*, 130075.

23. Nam, I.; Kim, G.-P.; Park, S.; Park, J.; Kim, N. D.; Yi, J. Fabrication and Design Equation of Film-Type Large-Scale Interdigitated Supercapacitor Chips. *Nanoscale* **2012**, *4*, 7350–7353.

24. Pech, D.; Brunet, M.; Durou, H.; Huang, P.; Mochalin, V.; Gogotsi, Y.; Taberna, P.-L.; Simon, P. Ultrahigh-Power Micrometre-Sized Supercapacitors Based on Onion-Like Carbon. *Nat. Nanotechnol.* **2010**, *5*, 651–654.

25. El-Kady, M. F.; Kaner, R. B. Scalable Fabrication of High-Power Graphene Micro-Supercapacitors for Flexible and On-Chip Energy Storage. *Nat. Commun.* **2013**, *4*, 1475.

26. Lia, T.; Suoa, Z.; Lacoura, S. P.; Wagner, S. Compliant Thin Film Patterns of Stiff Materials as Platforms for Stretchable Electronics. *J. Mater. Res.* **2005**, *20*, 3274.

27. Lu, W.; Henry, K.; Turchi, C.; Pellegrino, J. Incorporating Ionic Liquid Electrolytes into Polymer Gels for Solid-State Ultracapacitors. *J. Electrochem. Soc.* **2008**, *155*, A361–A367.

28. Masarapu, C.; Zeng, H. F.; Hung, K. H.; Wei, B. Effect of Temperature on the Capacitance of Carbon Nanotube Supercapacitors. *ACS Nano* **2009**, *3*, 2199–2206.

29. Wu, Z.-S.; Parvez, K.; Feng, X.; Müllen, K. Graphene-Based In-Plane Micro-Supercapacitors with High Power and Energy Densities. *Nat. Commun.* **2013**, *4*, 2487.

30. Hu, C.-C.; Chang, K.-H.; Lin, M.-C.; Wu, Y.-T. Design and Tailoring of the Nanotubular Arrayed Architecture of Hydrous RuO_2 for Next Generation Supercapacitors. *Nano Lett.* **2006**, *6*, 2690–2695.

31. Wu, Z.-S.; Wang, D.-W.; Ren, W.; Zhao, J.; Zhou, G.; Li, F.; Cheng, H.-M. Anchoring Hydrous RuO_2 on Graphene Sheets for High-Performance Electrochemical Capacitors. *Adv. Funct. Mater.* **2010**, *20*, 3595–3602.

32. Kim, J.-H.; Zhu, K.; Yan, Y.; Perkins, C. L.; Frank, A. J. Microstructure and Pseudocapacitive Properties of Electrodes Constructed of Oriented NiO-TiO_2 Nanotube Arrays. *Nano Lett.* **2010**, *10*, 4099–4104.

33. Lu, Q.; Lattanzi, M. W.; Chen, Y.; Kou, X.; Li, W.; Fan, X.; Unruh, K. M.; Chen, J. G.; Xiao, J. Q. Supercapacitor Electrodes with High-Energy and Power Densities Prepared from Monolithic NiO/Ni Nanocomposites. *Angew. Chem.* **2011**, *123*, 6979–6982.

34. Yan, W.; Ayvazian, T.; Kim, J.; Liu, Y.; Donavan, K. C.; Xing, W.; Yang, Y.; Hemminger, J. C.; Penner, R. M. Mesoporous Manganese Oxide Nanowires for High-Capacity, High-Rate, Hybrid Electrical Energy Storage. *ACS Nano* **2011**, *5*, 8275–8287.

35. Wu, Z.-S.; Ren, W.; Wang, D.-W.; Li, F.; Liu, B.; Cheng, H.-M. High-Energy MnO_2 Nanowire/Graphene and Graphene Asymmetric Electrochemical Capacitors. *ACS Nano* **2010**, *4*, 5835–5842.

36. Li, Q.; Wang, Z.-L.; Li, G.-R.; Guo, R.; Ding, L.-X.; Tong, Y.-X. Design and Synthesis of MnO_2/Mn/MnO_2 Sandwich-Structured Nanotube Arrays with High Supercapacitive Performance for Electrochemical Energy Storage. *Nano Lett.* **2012**, *12*, 3803–3807.

37. Jiang, H.; Zhao, T.; Yan, C.; Ma, J.; Li, C. Hydrothermal Synthesis of Novel Mn_3O_4 Nano-Octahedrons with Enhanced Supercapacitors Performances. *Nanoscale* **2010**, *2*, 2195–2198.

38. Lee, G.; Kim, D.; Yun, J.; Ko, Y.; Cho, J.; Ha, J. S. High-Performance All-Solid-State Flexible Micro-Supercapacitor Arrays with Layer-by-Layer Assembled MWNT/MnO_x Nanocomposite Electrodes. *Nanoscale* **2014**, *6*, 9655–9664.

39. Kim, D.; Shin, G.; Kang, Y. J.; Kim, W.; Ha, J. S. Fabrication of a Stretchable Solid-State Micro-Supercapacitor Array. *ACS Nano* **2013**, *7*, 7975–7982.

40. Cheng, S.; Wu, Z. Microfluidic Electronics. *Lab Chip* **2012**, *12*, 2782–2791.

41. Manly. M. D. *Fundamentals of Liquid Metal Corrosion*; Oak Ridge National Laboratory: Oak Ridge, TN, 1956; pp 1–10.

42. Lee, S. W.; Kim, B. S.; Chen, S.; Yang, S. H.; Hammond, P. T. Layer-by-Layer Assembly of All Carbon Nanotube Ultrathin Films for Electrochemical Applications. *J. Am. Chem. Soc.* **2009**, *131*, 671–679.

43. Ahmad, T.; Ramanujachary, K. V.; Lofland, S. E.; Ganguli, A. K. Nanorods of Manganese Oxalate: A Single Source Precursor to Different Manganese Oxide Nanoparticles (MnO, Mn_2O_3, Mn_3O_4). *J. Mater. Chem.* **2004**, *14*, 3406–3410.

44. An, G.; Yu, P.; Xiao, M.; Liu, Z.; Miao, Z.; Ding, K.; Mao, L. Low-Temperature Synthesis of Mn_3O_4 Nanoparticles Loaded on Multi-Walled Carbon Nanotubes and Their Application in Electrochemical Capacitors. *Nanotechnology* **2008**, *19*, 27570.

45. Zhang, H.; Cao, G.; Wang, Z.; Yang, Y.; Shi, Z.; Gu, Z. Growth of Manganese Oxide Nanoflowers on Vertically-Aligned Carbon Nanotube Arrays for High-Rate Electrochemical Capacitve Energy Storage. *Nano Lett.* **2008**, *8*, 2664–2668.

46. Ye, J. S.; Cui, H. F.; Liu, X.; Lim, T. M.; Zhang, W. D.; Sheu, F. S. Preparation and Characterization of Aligned Carbon Nanotube-Ruthenium Oxide Nanocomposites for Supercapacitors. *Small* **2005**, *1*, 560–565.

47. Zhang, H.; Cao, G.; Yang, Y. Electrochemical Properties of Ultra-Long, Aligned, Carbon Nanotube Array Electrode in Organic Electrolyte. *J. Power Sources* **2007**, *172*, 476–480.

48. Taberna, P. L.; Simon, P.; Fauvarque, J. F. Electrochemical Characteristics and Impedance Spectroscopy Studies of Carbon-Carbon Supercapacitors. *J. Electrochem. Soc.* **2003**, *150*, A292–A300.

49. Xiao, X.; Li, T.; Yang, P.; Gao, Y.; Jin, H.; Ni, W.; Zhan, W.; Zhang, X.; Cao, Y.; Zhong, J.; *et al.* Fiber-Based All-Solid-State Flexible Supercapacitors for Self-Powered Systems. *ACS Nano* **2012**, *6*, 9200–9206.

50. *ABAQUS Version 6.10 User's Manual*; Hibbitt, Karlson & Sorensen: Providence, RI, 2012.

51. Jung, J. H.; Lee, M.; Hong, J.-I.; Ding, Y.; Chen, C.-Y.; Chou, L.-J.; Wang, Z. L. Lead-Free $NaNbO_3$ Nanowires for a High Output Piezoelectric Nanogenerator. *ACS Nano* **2011**, *5*, 10041–10046.

52. Atieh, A.; Kalantari, M.; Ahmadi, R.; Dargahi, J.; Packirisamy, M.; Zadeh, M. H. FEM Analysis of the Interaction between a Piezoresistive Tactile Sensor and Biological Tissues. *World Acad. Sci. Eng. Tech.* **2011**, *5*, 909.

53. Azaïs, P.; Duclaux, L.; Florian, P.; Massiot, D.; L.-Rodenas, M.-A.; L.-Solano, A.; Peres, J.-P.; Jehoulet, C.; Béguin, F. Causes of Supercapacitors Ageing in Organic Electrolyte. *J. Power Sources* **2007**, *171*, 1046–1053.